High Rate Performance of Aqueous Magnesium-iron-ion Batteries Based on Fe_2O_3@GH as the Anode①

SHAO Shuang-Xi② CANG Rui-Bai② YE Ke③ GAO Yin-Yi
ZHU Kai YAN Jun WANG Gui-Ling CAO Dian-Xue③
(*Key Laboratory of Superlight Materials and Surface Technology of Ministry of Education, College of Materials Science and Chemical Engineering, Harbin Engineering University, Harbin* 150001, *China*)

ABSTRACT Aqueous Mg-ion batteries (MIBs) are safe, non-toxic and low-cost. Magnesium has a high theoretical specific capacity with its ion radius close to that of lithium. Therefore, aqueous magnesium ion batteries have great research advantages in green energy. To acquire the best electrode materials for aqueous magnesium ion batteries, it is necessary for the structural design in material. Fe_2O_3 is an anode material commonly used in Li-ion battery. However, the nano-cube Fe_2O_3 combined with graphene hydrogels (GH) can be successfully prepared and employed as an anode, which is seldom researched in the aqueous batteries system. The Fe_2O_3/GH is used as anode in the dual $MgSO_4$ + $FeSO_4$ aqueous electrolyte, avoiding the irreversible deintercalation of magnesium ions. In addition, the Fe element in anode material can form the Fe^{3+}/Fe^{2+} and Fe^{2+}/Fe^{3+} redox pairs in the $MgSO_4$ + $FeSO_4$ electrolyte. Thus, the reversible insertion/(de)insertion of magnesium and iron ions into/from the host anode material can be simultaneously achieved. After the initial charge, the anodic structure is changed to be more stable, avoiding the formation of MgO. The Fe_2O_3/GH demonstrates high rate properties and reversible capacities of 198, 151, 121, 80, 75 and 27 mAh g^{-1} at 50, 100, 200, 300, 500 and 1000 mA g^{-1} correspondingly.

Keywords: aqueous battery, Mg ion, Fe_2O_3/graphene hydrogels, anode material, $FeSO_4$;
DOI: 10.14102/j.cnki.0254–5861.2011–3063

1 INTRODUCTION

Recently, magnesium ion battery has aroused more and more attention, in which not only the ion radius of magnesium is similar to that of lithium but also magnesium is low cost and abundant resources on the earth. Aqueous Mg-ion batteries (MIBs) attract much attention due to their high theoretical capacity and abundant resource[1]. The aqueous MIBs play an important role in the development of green energy compared with no-aqueous MIBs[2], because of their advantages of low cost, safety, stability, and sustainable development. The aqueous MIBs electrolyte comes from aqueous and inorganic magnesium salt. Since the first aqueous rechargeable battery was produced by SONY in 1994[3], most cathode materials such as MnO_2, $LiMn_2O_4$ and $Na_{0.44}MnO_2$ have been used in lithium/sodium battery[4−8]. For the development of cathode materials, various cathode materials such as transition metal chalcogenides/oxides, polyanion compounds, and Prussian blue are synthesized as a capable host for Mg ion storage[9]. Among them, manganese oxide has become an interesting research subject and a capable host for MIBs owing to its high capacity (~200 mAh g^{-1}), suitable working voltage and low cost[10−12]. In contrast, the progress in anode materials is slow and lack of capable anode materials, which seriously hinders the potential applications of aqueous MIBs[13−16]. Zhang et al. reported $FeVO_4$ nanomaterials as anodes for aqueous MIBs with a capacity of 140 mAh g^{-1}[17]. Unfortunately, their low capacity is difficult to match with manganese oxide cathode well and the structural collapse of pure materials results in a continuous

Received 10 December 2020; accepted 7 January 2021
① This project was supported by the National Natural Science Foundation of China (51672056), the Excellent Youth Project of the Natural Science Foundation of Heilongjiang Province (YQ2019B002) and the Fundamental Research Funds for the Central Universities
② These authors contributed equally to this work
③ Corresponding authors. E-mails: yeke@hrbeu.edu.cn (Ye K.) and caodianxue@hrbeu.edu.cn (Cao, D. X)

capacity decay during the Mg (de)intercalation process. Thus, there is a challenge to identify an inexpensive anode with a large capacity and highly reversible charge storage mechanism in an aqueous electrolyte[18−20]. The controlled morphology of materials can effectively improve the electrochemical properties of materials. Nano Fe_2O_3 materials with special cubic structures because of its high theoretical capacity are used as an anode material having excellent properties (924 mAh g^{-1}), low cost, low toxicity and natural abundance of iron[21−23]. Unfortunately, lithiation large volume expansion, poor electronic conductivity and ion diffusion capacity are major problems limiting the practical applicability of these negative electrode materials[24, 25].

According to the reports, the design and manufacture of particles have a special form and customized performance that can be enhanced by cycling performance and rate capability. The Fe_2O_3-based anode materials were used in the non-aqueous battery, because iron metal batteries are extremely competitive in their cost and iron possesses an attractive electrochemical property. Via the two-electron transfer, iron theoretically delivers a high specific capacity of ~960 mAh g^{-1} and an outstanding volumetric capacity of ~7557 mAh cm^{-3}, both of which are higher than those for other electrode materials like P_2-$Mg_{1/3}Ni_{1/3}Mn_{2/3}O_2$ electrode at 1.0 C in 1.0 M $MgSO_4$ (101.4 mAh g^{-1}), $Mg(NO_3)_2$ (99.7 mAh g^{-1}), and $MgCl_2$ (117.0 mAh g^{-1}) electrolytes and $NaTi(PO_4)_3$ as an anode at 0.78 C in 1.0 M $NaNO_3$ electrolyte (121 mAh g^{-1})[26, 27]. However, when the Fe_2O_3-based materials were used as anode or Fe_2O_3 as a cathode in aqueous MIBs, the magnesium ion can't insert/(de)insert in Fe_2O_3 but can only stick to Fe_2O_3. The above-mentioned iron-base anode materials show considerable interests on the Fe-metal flow batteries, where the cathode and anode operate on the Fe^{3+}/Fe^{2+} and Fe^{2+}/Fe^{3+} redox couples, respectively. Herein, we prepared the Fe_2O_3 and Fe_2O_3/graphene hydrogels (GH) anodes. The Fe_2O_3/GH displayed a capacity of 198 mAh g^{-1} in the aqueous $MgSO_4$ + $FeSO_4$ electrolyte for Mg-Fe ion battery, indicating an excellent storage capacity of magnesium and iron ions. All the above clearly reveal that Fe_2O_3/GH is an excellent anode material for high-performance Mg-Fe-ion battery and an important step in the development of an aqueous Mg-Fe-ion battery. This battery shows higher rate properties than other aqueous batteries[28−30], delivering the reversible capacity of 198 mAh g^{-1} at a current density of 50 mA g^{-1}. This result also lays theoretical foundation for the application of aqueous magnesium-iron ion batteries.

2 EXPERIMENTAL

2. 1 Preparation and characterization of Fe_2O_3 and Fe_2O_3/GH

The typical synthesis of $FeCl_3$ $6H_2O$ was dissolved in ethanol and DI water under vigorously magnetic stirring, during which sodium acetate was added until complete dissolution. Then, the mixture was sealed in a Teflon-lined stainless-steel autoclave and maintained at 180 ℃ for 12 h. After cooling to room temperature, the products were formed as red solation and washed several times by DI water and ethanol, and the final dark red products were dried at 60 ℃ for overnight. Subsequently, the obtained Fe_2O_3/GH was utilized for fabricating Fe_2O_3/GH composite. The process of recombination of Fe_2O_3 and graphene composite is as follows. Firstly, for the preparation of solution A, graphene oxide was dissolved in DI-water and added into ethylenediamine with good stirring and even distribution. Secondly, Fe_2O_3 nanocubes were dissolved in DI-water to form solution B. Thirdly, solutions A and B were mixed and fully ultrasonicated to make the Fe_2O_3 nano-cubes uniformly disperse in the mixed solution (Scheme 1). Such a self-assembled composite is advantageous in the cubic structure of Fe_2O_3 nanoparticles and graphene can keep its original topography. Furthermore, it is noted that, after a hydrothermal reaction by freeze-drying procedures. The microstructure of composite can be easily controlled by graphene oxide, because the graphene sheet with a high surface area can effectively prevent the aggregation of Fe_2O_3 nanocube. Furthermore, the addition of Fe_2O_3 can effectively prevent the accumulation of graphene sheets, which can obtain the composite material with a high surface area. Meantime, the Fe_2O_3/GH nano-cubes composite with loose porous structure by freeze-drying process can enhance pore volume. Fe_2O_3/GH composite material having a high surface area and high electrical conductivity is a promising electrode material, so it can provide a large surface area of electrochemical reaction and discharging/charging process to provide several active Mg and Fe ion diffusions.

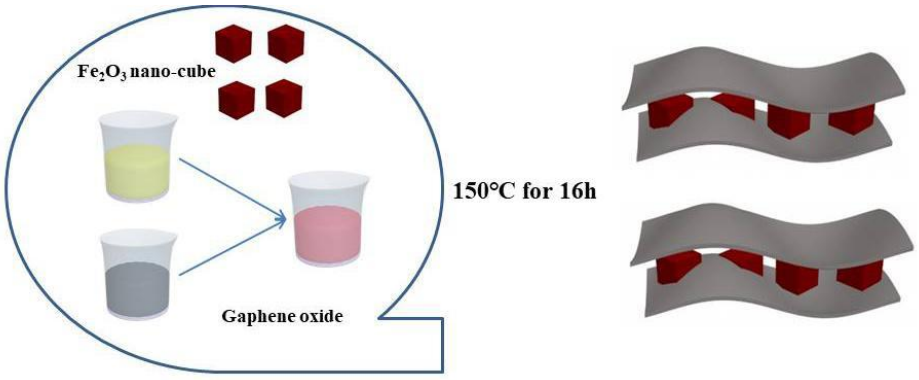

Scheme 1. An illustration for the formation of Fe_2O_3/GH

2. 2 Electrochemical measurement of Fe_2O_3 and Fe_2O_3/GH

The slurry of the anode was constituted by mixing 10% polyvinylidene difluoride (PVDF) binder, 10% acetylene black and 80% Fe_2O_3 and Fe_2O_3/GH. The carbon fiber cloth with a size of 1.2 cm × 1.2 cm is used to coat the above slurry under vacuum drying at 80 ℃ for 24 h.

3 RESULTS AND DISCUSSION

X-ray diffraction (XRD) gives the institute composite phase structure and phase purity (Fig. 1). The major diffraction peaks of Fe_2O_3 (brown line) and Fe_2O_3/GH (ginger line) can be well indexed to the phase of Fe_2O_3 (hematite, JCPDS33-0664). Comparing these two curves, the contrast between Fe_2O_3/GH and Fe_2O_3 shows a new peak at about 26.6, which is from graphene[31]. This result proves that Fe_2O_3/graphene hydrogel (GH) successfully recombines.

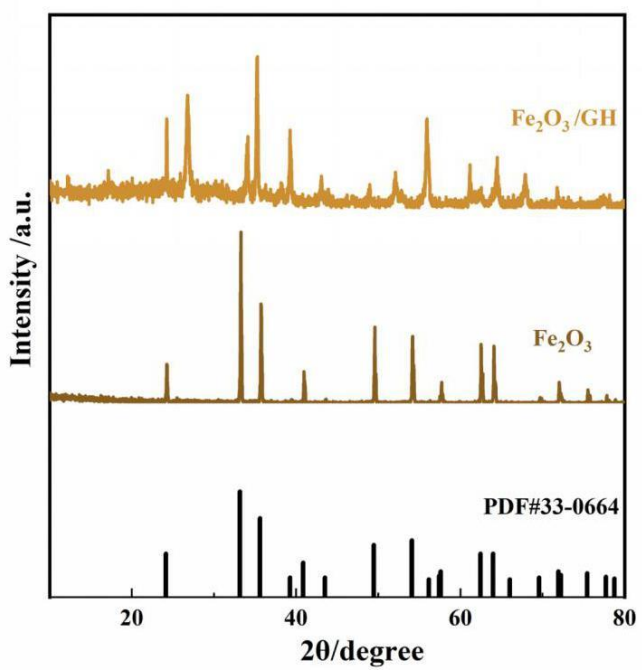

Fig. 1. XRD patterns of Fe_2O_3 and Fe_2O_3/GH

It has come to light that graphene is an electrode material with high conductivity and large specific surface area. Therefore, we prepared the Fe_2O_3 and graphene composite using as an anode to improve the electrochemical properties. Fig. 2 shows the SEM images of Fe_2O_3 and Fe_2O_3/GH. In Figs. 2a and 2b, Fe_2O_3 is the regular cube material. In Figs. 2c and 2d, the Fe_2O_3 anode materials demonstrate an average size less than 100 nm. Figs. 2e and 2f show the Fe_2O_3/GH image. A graphene sheet structure is clearly visible and the Fe_2O_3 is non-uniformly distributed on the sheet.

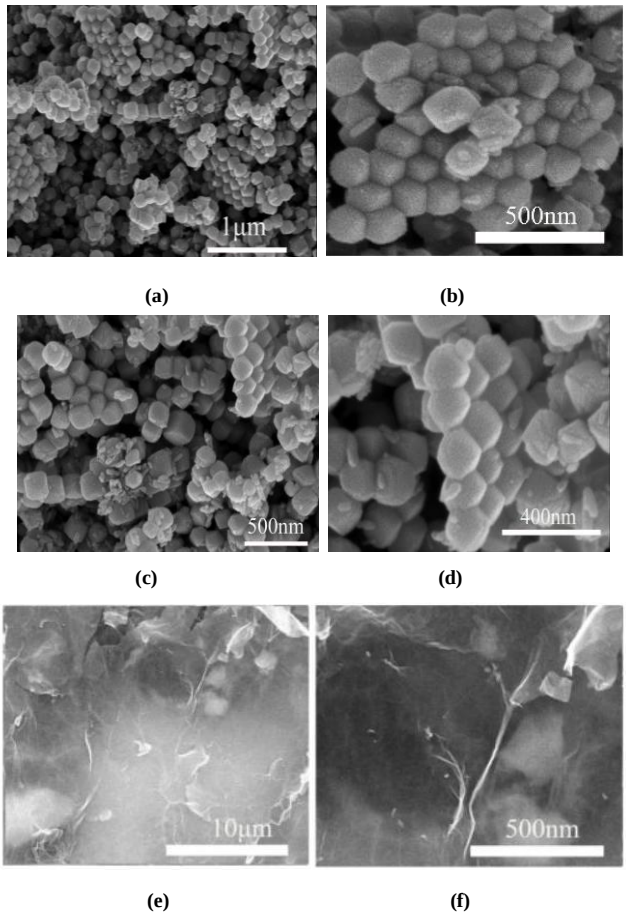

Fig. 2. SEM images of Fe_2O_3 (a∼d) and Fe_2O_3/GH (e∼f)

Fe_2O_3 and Fe_2O_3/GH are used as an anode material in 0.5 M $MgSO_4$ and 0.5 M $MgSO_4$ + $FeSO_4$ aqueous electrolyte for the working electrode. The cyclic voltammetry (CV) curves of Fe_2O_3 and Fe_2O_3/GH electrodes with a voltage window of –1.1∼0.5 V at a scan rate of 3.0 mV s^{-1} are shown in Fig. 3. Fig. 3a displays the Fe_2O_3 as an anode in 0.5 M $MgSO_4$ aqueous solution, showing a cathodic peak at 0.0 V and three anodic peaks at –0.38, –0.30 and 0.08 V, respectively. In the CV curves, Mg ion is inserted in the electrode material, but Mg ion can't insert/(de)insert in the Fe_2O_3 nano-cube material during charge and discharge process. Fig. 3b shows the Fe_2O_3 anode materials in 0.5 M $MgSO_4$ + $FeSO_4$ aqueous solution, which has only two cathodic peaks at 0.26/–0.18 V and an anodic peak at –0.86 V. The whole peak-current potential shifts to the left direction with an obvious planning phenomenon. To further solve the above problems, the Fe_2O_3/GH was used as an anode in 0.5 M $MgSO_4$ (Fig. 3c), which had two cathodic peaks at 0.15/–0.30 V and an anodic peak at –0.78 V with the polarization phenomenon disappearing significantly. The anode is still a quasi-reversible process, because Mg ion is only inserted at the Fe_2O_3 material in discharge. During charging, the Mg ions can't be released from the Fe_2O_3 material to form an irreversible state. Fig. 3d shows the Fe_2O_3/GH as an anode in $MgSO_4$ + $FeSO_4$ with a reversible system, which has two anodic peaks at –0.6/–0.3 V and cathodic peaks at –0.16/–0.46 V with potentials in safe voltage ranges. The insertion/(de)insertion process of Mg and Fe ions into/from Fe_2O_3/GH material results from the donor and acceptor of electrons accompanied with Mg^{2+} ion insertion/(de)insertion process into/from the lattice of Fe_2O_3/GH, in which the catholyte and anolyte operate on Fe^{2+}/Fe^{3+} with the multi-step Mg/Fe-ion storage process. Electrochemical kinetics of the reaction at particular electrode can be determined from the voltage difference between the redox peaks. The Fe_2O_3 was used as an anode in $MgSO_4$ and $MgSO_4$ + $FeSO_4$ aqueous solution, and the voltage gaps between the redox peaks are 0.51 and 0.81 V, respectively. For Fe_2O_3/GH as an anode in $MgSO_4$ and $MgSO_4$ + $FeSO_4$ aqueous solution, the voltage gaps between the redox peaks are 0.72 and 0.51 V, respectively. Thus, the Fe_2O_3/GH in $MgSO_4$ + $FeSO_4$ decreased the electrode

polarization, which is advantageous for the electrochemical reaction. Meanwhile, the Fe_2O_3/GH anode materials in $MgSO_4$ + $FeSO_4$ reveal preferable electrochemical properties than other electrodes according to the peak currents.

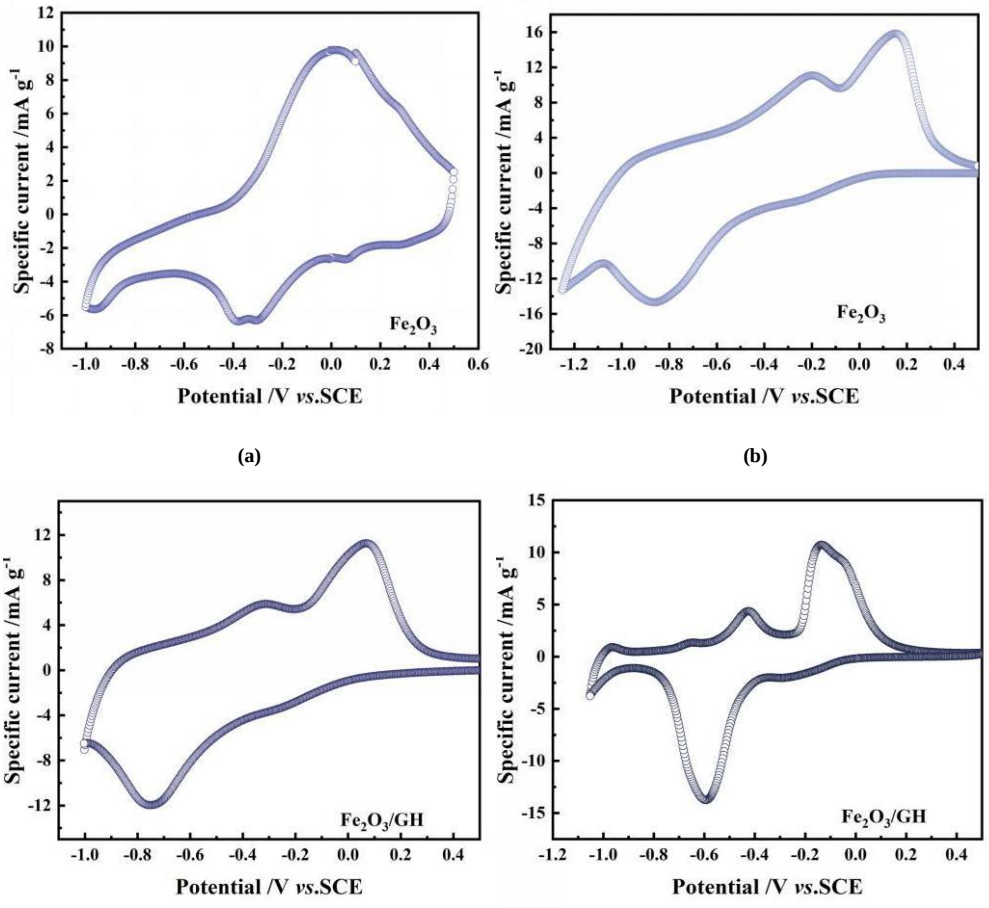

Fig. 3. CVs of Fe_2O_3 electrode in 0.5 M $MgSO_4$ (a) and 0.5 M $MgSO_4$ + $FeSO_4$ (b) electrolyte, respectively; Fe_2O_3/GH electrode in 0.5 M $MgSO_4$ (c) and 0.5 M $MgSO_4$ + $FeSO_4$ (d) electrolyte, respectively

To further study the electrochemical properties of Fe_2O_3 and Fe_2O_3/GH, the galvanostatic charge-discharge measurements were tested in the voltage window of –1.0 to 0.4 V. Fig. 4a shows the Fe_2O_3 as an anode at 100 mA g^{-1} with the initial cycle discharge specific capacity of 38 mAh g^{-1} in 0.5 M $MgSO_4$ and the coulombic efficiency close to 100%. In addition, Fe_2O_3 was used as anode within the voltage window of –0.85 to 0.1 V in $MgSO_4$ + $FeSO_4$ at 100 mA g^{-1} and its discharge specific capacity was 131 mAh g^{-1} (Fig. 4b). Although there is a certain improvement in specific capacity, the coulombic efficiency is weak with 91%. The discharge/charge curves of Fe_2O_3/GH as an anode in $MgSO_4$ with the capacity of 400 mAh g^{-1} and coulombic efficiency of 62.5% are shown in Fig. 4c. After improving the conductivity of the electrode, the capacity is increased and verified before CV test. Mg ion is only inserted in the Fe_2O_3 material in discharge. During the charging process, Mg ion can't be released from the iron material to form an irreversible state. When the Fe_2O_3/GH was used as an anode in $MgSO_4$ + $FeSO_4$, it had an outstanding performance with the discharge specific capacity of 155 mAh g^{-1} and coulombic efficiency close to 100% at a current density of 100 mA g^{-1}. Meanwhile, the potential of the discharge plateau is almost identical to that of CV. The Fe_2O_3/GH as an anode in 0.5 M $MgSO_4$ + $FeSO_4$ aqueous solution can not only avoid the phenomenon of hydrogen and oxygen evolution but also improve the electrochemical performance and stability to a certain extent.

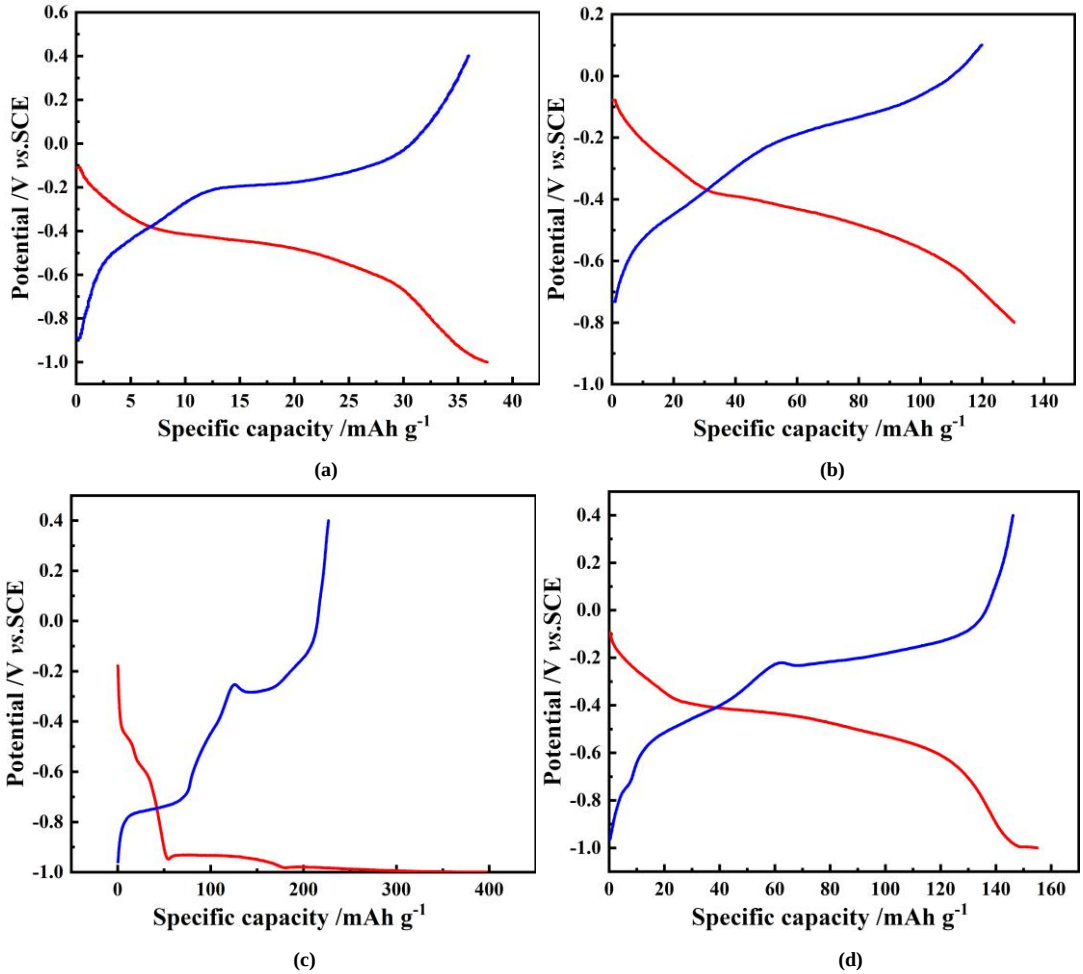

Fig. 4. Galvanostatic charge and discharge curves of Fe_2O_3 anode in 0.5 M $MgSO_4$ (a) and 0.5 M $MgSO_4$ + $FeSO_4$ (b) electrolyte, respectively; Fe_2O_3/GH anode in 0.5 M $MgSO_4$ (c) and 0.5 M $MgSO_4$ + $FeSO_4$ (d) electrolyte, respectively

Electrochemical impedance spectroscopic (EIS) measurement of Fe_2O_3 and Fe_2O_3/GH in $MgSO_4$ + $FeSO_4$ is shown in Fig. 5. The main purpose of the EIS test is to further verify the diffusion rate of the Fe_2O_3 and Fe_2O_3/GH material in the electrolyte at room temperature. Fig. 5a shows the impedance spectra of Fe_2O_3 and Fe_2O_3/GH electrodes. In the high-frequency region, the partial semicircle indicates a charge transfer resistance (R_{ct}) and the intercept indicates the internal resistance (R_s). In low-frequency region, the linear portion represents the Warburg impedance, which is utilized to determine the diffusion coefficient of magnesium-iron ions in the electrode. Therefore, the model circuit (inset of Fig. 5a) is fitted by ZView software and the relevant parameters are listed in Table 1. Fig. 5b shows the curve of Z_{Re} as a function of $\omega^{-1/2}$, depending on the slope of linear portion of the low-frequency region. Therefore, the magnesium-iron ion diffusion coefficient (D_{Mg2+}) can be obtained by Eqs. (1) and (2) as below:

$$D_{Mg^{2+}} = \frac{R^2T^2}{2A^2n^4F^4C^2\sigma^2} \quad (1)$$

$$Z_{Re} = R_s + R_{ct} + \sigma\omega^{-1/2} \quad (2)$$

where D_{Mg2+} is the magnesium-iron ion diffusion coefficient ($cm^2\ s^{-1}$), F is the Faraday constant, R is the gas constant, T is the room temperature (25 ℃), A is the surface area of the electrode, n is the number of transferred electrons (n = 1), σ is the slope of Z_{Re} against $\omega^{-1/2}$ plot, and C is the concentration of the magnesium-iron ion.

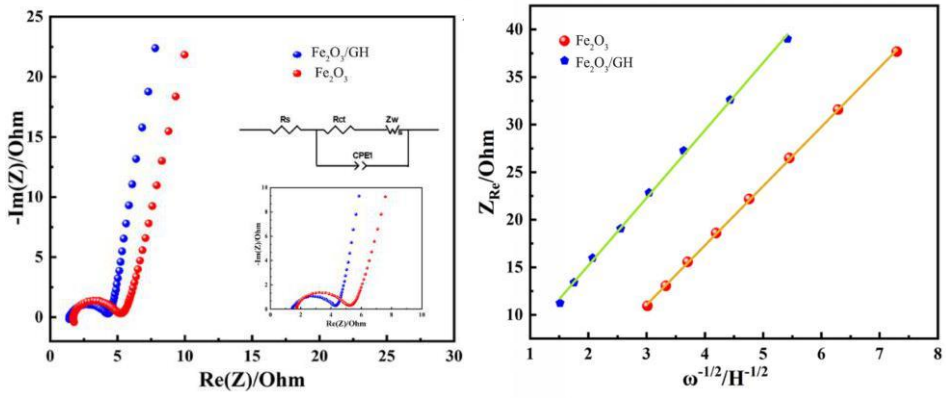

(a) **(b)**

Fig. 5. Impedance spectra of the Fe_2O_3 and Fe_2O_3/GH electrodes (a); the slope of Z_{Re} against $\omega^{-1/2}$ plot (b)

In Table 1, the internal resistance R_s values of the two electrodes are a little different. The charge-transfer resistance R_{ct} value of Fe_2O_3/GH is much smaller than that of the Fe_2O_3 electrode, because the Fe_2O_3/GH composite owns a larger specific surface area and higher electrical conductivity derived from the GH property and more beneficial for the charging process. Z_{Re} is derived from Eq. (2) and the diffusion coefficient D_{Mg2+} can be calculated from Eq. (1). The D_{Mg}^{2+} value of Fe_2O_3/GH electrode is much larger than that of the Fe_2O_3 electrode, proving that magnesium-iron ions diffuse faster onto the surface of electrode. In consequence, R_s and R_{ct} of the Fe_2O_3/GH electrode shows a smaller value. The large D_{Mg}^{2+} value indicates a good electrochemical kinetics.

Table 1. Evaluated Impedance Parameter Values of the Two Electrodes in 0.5 M $MgSO_4$ + $FeSO_4$ Electrolyte from EIS of Fig. 5

Sample	R_s (Ω)	DMg^{2+} ($cm^2\ s^{-1}$) ±0.01 E^{-15}	CPE-T	CPE-P	Sample
Fe_2O_3	3.52	8.88 E^{-15}	9.23 E^{-5}	0.98	Fe_2O_3
Fe_2O_3/GH	3.16	9.65 E^{-15}	9.77 E^{-5}	0.90	Fe_2O_3/GH

The Fe_2O_3/GH anode displays a high rate capability and superior cycle ability. Fig. 6 shows the Fe_2O_3/GH electrode charge/discharges in the potential region from –1.0 to 0.4 V at different currents in $MgSO_4$ + $FeSO_4$ electrolyte. Fig. 6a depicts the rate performance of Fe_2O_3/GH as an anode. The Fe_2O_3/GH exhibits the capacities of 198, 155, 121, 80, 75 and 27 mAh g^{-1} at 50, 100, 200, 300, 500 and 1000 mA g^{-1}, respectively. All the discharge curves in Mg-Fe ion electrolyte exhibit a large potential plateau at around –0.4 and –0.6 V, which are associated with the insertion of Mg^{2+} into the lattice of Fe_2O_3/GH and the process of Fe^{3+} to Fe^{2+}. The charge potential plateau appears at around –0.2 and 0.1 V, which are associated with the (de)insertion of Mg^{2+} from the lattice of Fe_2O_3/GH and process of Fe^{2+} to Fe^{3+}, demonstrating a capable rate performance of Fe_2O_3/GH as an anode in 0.5 M $MgSO_4$ + $FeSO_4$ aqueous solution. Meanwhile, at a current density of 100 mA g^{-1}, Fe_2O_3/GH anode exhibits a discharge specific capacity of 165 mAh g^{-1} at the initial cycle with a capacity retention of 89.3% after 200 cycles, suggesting an outstanding cycling stability (Fig. 6c). It is noted that, after 200 cycles, the respective capacity retention is close to 100%, demonstrating the most excellent cycle stability in $MgSO_4$ + $FeSO_4$ aqueous solution. The Mg-Fe ions are converted into the insertion without structural collapse with a reversible process. The electrochemical performance is prior to that of other aqueous-based batteries, such as 150 mAh g^{-1} of Mg-bir/CC in 0.5 M $Mg(ClO_4)_2$[31], 90 mAh g^{-1} of 400-$MgMn_2O_4$ in 3.0 M $Mg(NO_3)_2$[32], 51 mAh g^{-1} of CuFe-PBA in 1.0 M $Mg(NO_3)_2$[33] and 59.2 mAh g^{-1} of polypyrrole (PPy)-coated MoO_3[34], which provides a new member for aqueous battery family (as listed in Table 2 and Table S1)[34–38].

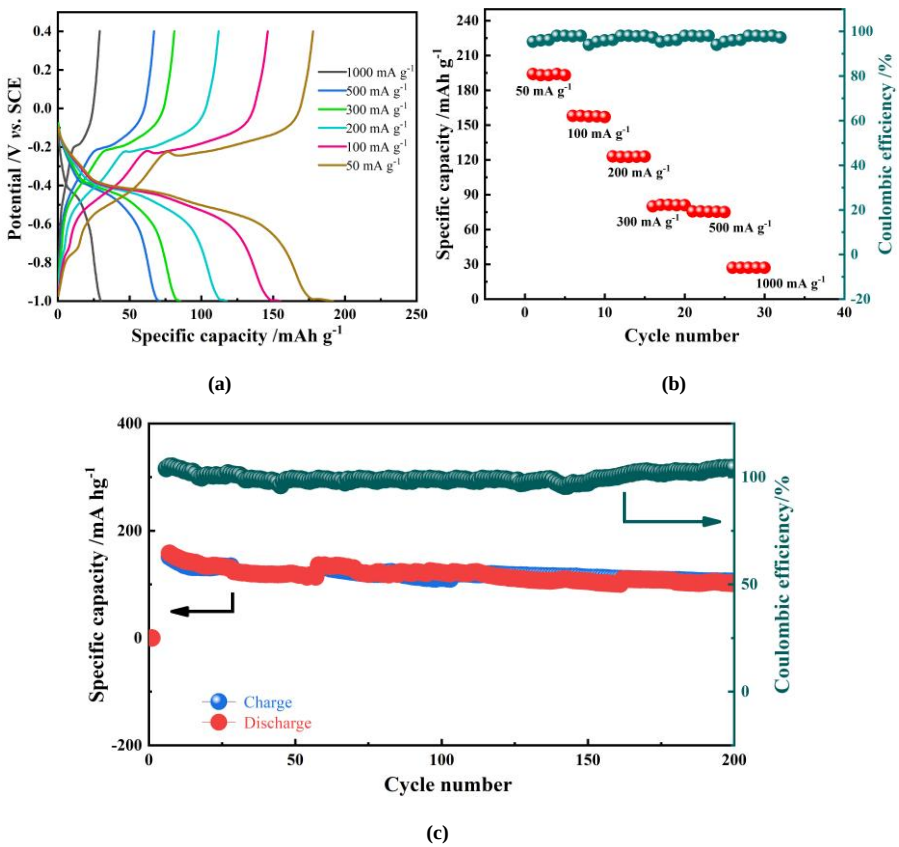

Fig. 6. Rate performance of Fe_2O_3/GH electrode (a and b); the cycle performance of Fe_2O_3/GH electrode (c) in 0.5 M $MgSO_4$ + $FeSO_4$ electrolyte

Table 2. Comparison of Our Rechargeable Battery with State-of-the-art Works in Terms of Electrode, Electrolyte and Capacity

Electrode	Electrolyte	Capacity (mAh g^{-1})	Ref.
TiO_2	Aqueous	75	12
Mg-bir/CC	$Mg(ClO_4)_2$	150	31
$Na_3V_2(PO_4)_3$	$NaNO_3$	112	36
(PPy)-coated/MoO_3	Aqueous	59	34
TiO_2/graphene	Aqueous	30	35
400-$MgMn_2O_4$	$Mg(NO_3)_2$	90	32
CuFe-PBA	$Mg(NO_3)_2$	51	33
$Na_2Ti(PO_4)_3$	$NaNO_3$	121	27
V_2O_5/GA	$MgSO_4$	75	21
$FeVO_4$	$MgSO_4$	118	17
Fe_2O_3/GH	$MgSO_4$ + $FeSO_4$	198	This work

In order to further determine the composition of the composite material and electrochemical reaction changes, XPS measurement is performed to explore the change of magnesium-iron ions during the charging and discharging process of Fe_2O_3/GH electrode. Fig. 7a shows the survey spectra of Fe_2O_3/GH electrodes of fresh (black line) and discharge to –1.0 V (red line). It was clearly observed that Mg 1*s*, Mg 2*s*, and Mg 2*p* are discovered in the discharge to –1.0 V, and the F 1*s* peak comes from PVDF and C 1*s* peak from acetylene black and graphene. Fig. 7b depicts the C1*s* XPS spectra can be divided into four peaks, centered at 284.0, 285.4, 288.3 and 291.8 eV, respectively. They are consistent with the references of C=C, C–O, sp^2-bonded C atoms and CF. The corresponding fraction of C=C bonding was almost the highest, revealing a deep deoxidation of graphene oxide. The CF comes from PVDF. As shown in Fig. 7c, the characteristic peaks in O 1*s* XPS spectra can be divided into three peaks. The peak at a binding energy of

529.0 eV represents an anion O^{2-} for Fe_2O_3 in the center. Another peak at 531.2 eV indicates the presence of non-hydroxyl equivalent (or chemically adsorbed water) and Fe_2O_3 on the surface of the oxygen ion in the anoxic zone, and the third peak at 532.8 eV is corresponding to C=O in GH. Fig. 7d shows the Mg 1*s* peak is located at 1303 eV for the reduced electrode that discharges to –1.0 V. It is proved that a large number of Mg^{2+} ions are inserted into the lattice of the Fe_2O_3/GH electrode after the discharge process. In Fig. 7e, the electrode was observed in fresh Fe 2*p* XPS spectra with two peaks at 725.4 and 711.4 eV. This electrode is not inserted into Fe_2O_3/GH for magnesium ions[17, 36] and in good agreement with the formation of Fe_2O_3. When the electrode discharges to –1.0 V, the weak Fe $2p_{3/2}$ and Fe $2p_{1/2}$ peaks at 719.0 eV correspond to the characteristic peaks and their shake-up satellite peak of Fe 2*p*, respectively.

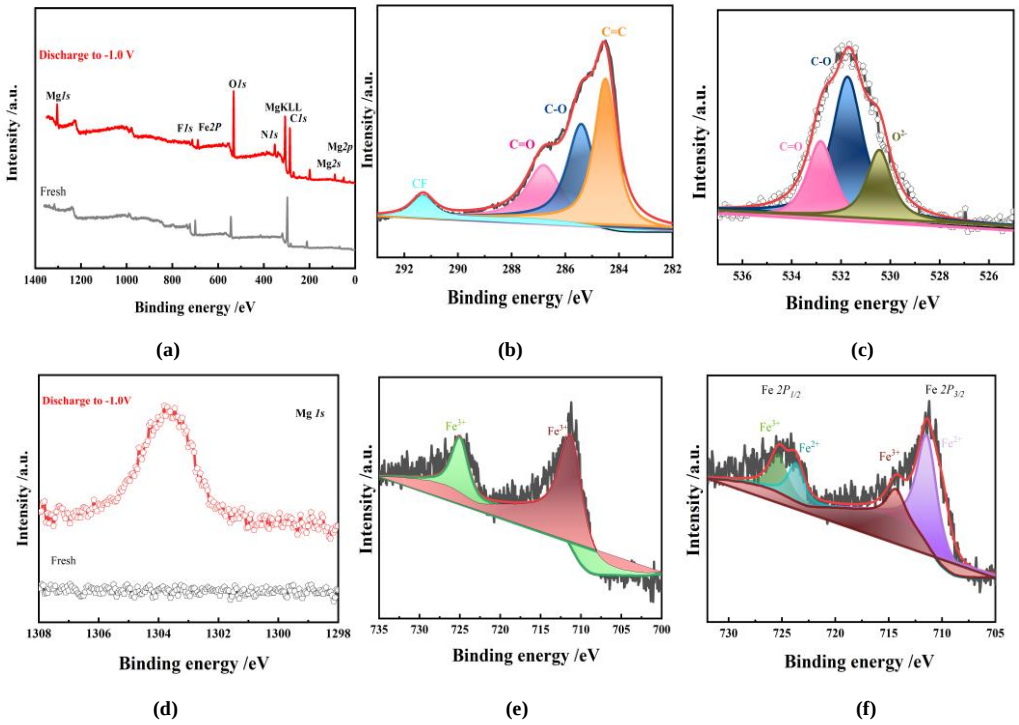

Fig. 7. XPS spectra of the fresh Fe_2O_3/GH and discharge to –1.0 V electrodes (a) and C 1*s* core level spectra of fresh (b), O1*s* core level spectra of fresh (c), and Mg 1*s* core level spectra (d), Fe 2*p* core level spectra of fresh (e) and discharge to –1.0 V electrode (f)

4 CONCLUSION

In this work, we introduced an anodic electrode of Fe_2O_3 in aqueous MIBs and recombined it with graphene hydrogels (GH) to form Fe_2O_3/GH. The Fe_2O_3 and Fe_2O_3/GH were electrochemically measured in different aqueous solutions. The Fe_2O_3 and Fe_2O_3/GH electrodes have overcome some problems such as the conservation of cycle stability and efficiency. The Fe_2O_3/GH as anode exhibits a high specific rate capacity and rate ability in 0.5 M $MgSO_4$ + $FeSO_4$. The charge/discharge specific capacity approaches to 86% capacity retention after 200 cycles, and the Fe_2O_3/GH electrode delivers a reversible capacity of 155 mAh g^{-1} at 100 mA g^{-1} with the coulombic efficiency close to 100%. Even at a high current density of 1000 mA g^{-1}, all electrochemical platforms remain unchanged, and the discharge specific capacity is 25 mAh g^{-1}. This material has not only a long cycle characteristic but also stable Coulomb efficiency, thus playing an important role in the construction of our green energy. For fixed or grid-level energy storage applications, it would be a viable alternative.

REFERENCES

(1) Whitacre, J. F.; Wiley, T.; Shanbhag, S.; Wenzhuo, Y.; Mohamed, A.; Chun, S. E.; Weber, E.; Blackwood, D.; Lynch-Bell, E.; Gulakowski, J.; Smith, C.; Humphreys, D. An aqueous electrolyte, sodium ion functional, large format energy storage device for stationary applications. *J. Power Sources* **2012**, 213, 255–264.

(2) Pang, G.; Yuan, C.; Nie, P.; Ding, B.; Zhu, J.; Zhang, X. Synthesis of NASICON-type structured $NaTi_2(PO_4)_3$-graphene nanocomposite as an

anode for aqueous rechargeable Na-ion batteries. *Nanoscal*e **2014**, 6, 6328–6334.

(3) Ferg, E.; Gummow, R.; De, K. A. Spinel anodes for lithium-ion batteries. *J. Electrochem. Soc*. **1994**, 141, L147–L150.

(4) Sauvage, F.; Baudrin, E.; Tarascon, J. M. Study of the potentiometric response towards sodium ions of $Na_{0.44-x}MnO_2$ for the development of selective sodium ion sensors. *Sensor. Actuat. B: Chem.* **2007**, 120, 638–644.

(5) An, Y.; Tian, Y.; Wei, C.; Jiang, H.; Xi, B.; Xiong, S.; Feng, J.; Qian, Y. Scalable and physical synthesis of 2*D* silicon from bulk layered alloy for lithium-ion batteries and lithium-metal batteries. *ACS Nano* **2019**, 13, 13690–13701.

(6) Li, Z.; Young, D.; Xiang, K.; Carter, W. C.; Chiang, Y. M. Towards high power high energy aqueous sodium-ion batteries: the $NaTi_2(PO_4)_3/Na_{0.44}MnO_2$ system. *Adv. Energy Mater.* **2013**, 3, 290–294.

(7) Song, W.; Ji, X.; Zhu, Y.; Zhu, H.; Li, F.; Chen, J.; Lu, F.; Yao, Y.; Banks C. E. Aqueous sodium-ion battery using a $Na_3V_2(PO_4)_3$ electrode. *ChemElectroChem.* **2014**, 1, 871–876.

(8) Yuan, C.; Zhang, Y.; Pan, Y.; Wang, G.; Cao, D. Investigation of the intercalation of polyvalent cations (Mg^{2+}, Zn^{2+}) into λ-MnO_2 for rechargeable aqueous battery. *Electrochim. Acta* **2014**, 116, 404–412.

(9) Wang, X.; Bommier, C.; Jian, Z.; Li, Z.; Chandrabose, R. S.; Rodriguez-Perez, I. A.; Greaney, P. A.; Ji, X. Hydronium-ion batteries with perylenetetracarboxylic dianhydride crystals as an electrode. *Angew. Chem. Int. Ed.* **2017**, 56, 2909–2913.

(10) Zhu, C.; Han, T.; Duoss, E. B.; Golobic, A. M.; Kuntz, J. D.; Spadaccini, C. M.; Worsley, M. A. Highly compressible 3*D* periodic graphene aerogel microlattices. *Nat. Commun*. **2015**, 6, 1–8.

(11) Alfaruqi, M. H.; Mathew, V.; Gim, J.; Kim, S.; Song, J.; Baboo, J. P.; Sun, H. C.; Kim, J. Electrochemically induced structural transformation in a γ-MnO_2 cathode of a high capacity zinc-ion battery system. *Chem. Mater.* **2015**, 27, 3609–3620.

(12) Sha, L.; Liu, T.; Ye, K.; Zhu, K.; Yan, J.; Yin, J.; Wang, G.; Cao, D. A heterogeneous interface on $NiS@Ni_3S_2/NiMoO_4$ heterostructures for efficient urea electrolysis. *J. Mater. Chem. A* **2020**, 8, 18055–18063.

(13) Luo, W.; Allen, M.; Raju, V.; Ji, X. An organic pigment as a high-performance cathode for sodium-ion batteries. *Adv. Energy Mater.* **2014**, 4, 554–559.

(14) Li, D.; Guo, W.; Li, Y.; Tang, Y.; Yan, J.; Meng, X.; Xia, M.; Gao, F.; Tunnel structured hollandite $K_{0.06}TiO_2$ microrods as the negative electrode for 2.4 V flexible all-solid-state asymmetric supercapacitors with high performance. *J. Power Sources* **2019**, 413, 34–41.

(15) Bančič, T.; Bitenc, J.; Pirnat, K.; Kopač, L. A.; Grdadolnik, J.; Randon, V. A.; Dominko, R. Electrochemical performance and redox mechanism of naphthalene-hydrazine diimide polymer as a cathode in magnesium battery. *J. Power Sources* **2018**, 395, 25–30.

(16) Ye, K.; Cao, A.; Shao, J.; Wang, G.; Si, R.; Ta, N.; Xiao, J.; Wang, G. Synergy effects on Sn–Cu alloy catalyst for efficient CO_2 electroreduction to formate with high mass activity. *Sci. Bull*. **2020**, 65, 711–719.

(17) Cang, R.; Ye, K.; Shao, S.; Zhu, K.; Yan, J.; Wang, G.; Cao, D. A new perylene-based tetracarboxylate as anode and $LiMn_2O_4$ as cathode in aqueous Mg–Li batteries with excellent capacity. *Chem. Eng. J.* **2021**, 405, 126783–126791.

(18) Chen, L.; Bao, J. L.; Dong, X.; Truhlar, D. G.; Wang, Y.; Wang, C.; Xia, Y. Aqueous Mg-ion battery based on polyimide anode and Prussian blue cathode. *ACS Energy Lett.* **2017**, 2, 1115–1121.

(19) Bitenc, J.; Pirnat, K.; Mali, G.; Novosel, B.; Vitanova, A. R.; Dominko, R. Poly(hydroquinoyl-benzoquinonyl sulfide) as an active material in Mg and Li organic batteries. *Electrochem. Commun*. **2016**, 69, 1–5.

(20) Dong, X.; Guo, Z.; Guo, Z.; Wang, Y.; Xia, Y. Organic batteries operated at −70 ℃. *Joule* **2018**, 2, 902–913.

(21) Zhang, H.; Ye, K.; Zhu, K.; Cang, R.; Yan, J.; Cheng, K.; Wang, G.; Cao, D. High-energy-density aqueous magnesium-ion battery based on a carbon-coated $FeVO_4$ anode and a Mg-OMS-1 cathode. *Chem. Eur. J.* **2017**, 23, 17118–17126.

(22) Ye, K.; Zhou, Z.; Shao, J.; Lin, L.; Gao, D.; Ta, N.; Si, R.; Wang, G.; Bao, X. *In situ* reconstruction of a hierarchical Sn–Cu/SnO_x core/shell catalyst for high-performance CO_2 electroreduction. *Angew. Chem. Int. Ed.* **2020**, 59, 4814–4821.

(23) Wang, F.; Fan, X.; Gao, T.; Sun, W.; Ma, Z.; Yang, C.; Han, F.; Xu, K.; Wang, C. High-voltage aqueous magnesium ion batteries. *ACS Central Sci*. **2017**, 3, 1121–1128.

(24) Tang, Y.; Chen, T.; Yu, S.; Qiao, Y.; Mu, S.; Hu, J.; Gao, F. Synthesis of graphene oxide anchored porous manganese sulfide nanocrystals *via* the nanoscale Kirkendall effect for supercapacitors. *J. Mater. Chem. A* **2015**, 3, 12913–12919.

(25) Wang, Y.; Cui, X.; Zhang, Y.; Zhang, L.; Gong, X.; Zheng, G. Energy storage: achieving high aqueous energy storage *via* hydrogen-generation passivation. *Adv. Mater*. **2016**, 28, 7626–7632.

(26) Cang, R.; Ye, K.; Zhu, K.; Yan, J.; Yin, J.; Cheng, K.; Wang, G.; Cao, D. Organic 3*D* interconnected graphene aerogel as cathode materials for

high-performance aqueous zinc ion battery. *J. Energy Chem.* **2020**, 45, 52–58.

(27) Sha, L.; Ye, K.; Yin, J.; Zhu, K.; Cheng, K.; Yan, J.; Wang, G.; Cao, D. *In situ* grown 3*D* hierarchical $MnCo_2O_{4.5}$@$Ni(OH)_2$ nanosheet arrays on Ni foam for efficient electrocatalytic urea oxidation. *Chem. Eng. J.* **2020**, 381, 122603–122611.

(28) Kundu, D.; Oberholzer, P.; Glaros, C.; Bouzid, A.; Tervoort, E.; Pasquarello, A.; Niederberger, M. An organic cathode for aqueous Zn-ion batteries: taming a unique phase evolution toward stable electrochemical cycling. *Chem. Mater.* **2018**, 30, 13–17.

(29) Sha, L.; Ye, K.; Wang, G.; Shao, J.; Zhu, K.; Cheng, K.; Yan, J.; Wang, G.; Cao, D. Rational design of $NiCo_2S_4$ nanowire arrays on nickel foam as highly efficient and durable electrocatalysts toward urea electrooxidation. *Chem. Eng. J.* **2019**, 359, 1652–1658.

(30) Cang, R.; Zhao, C.; Ye, K.; Yin, J.; Zhu, K.; Yan, J.; Wang, G.; Cao, D. Aqueous calcium-ion battery based on a mesoporous organic anode and a manganite cathode with long cycling performance. *ChemSusChem.* **2020**, 13, 3911–3918.

(31) Rodr ́guez-P ́rez, I. A.; Yuan, Y.; Bommier, C.; Wang, X.; Ma, L.; Leonard, D. P.; Lerner, M. M.; Carter, R. G.; Wu, T.; Greaney, A.; Lu, J.; Ji, X. Mg-ion battery electrode: an organic solid's herring bone structure squeezed upon Mg-ion insertion. *J. Am. Chem. Soc.* **2017**,139, 313–322.

(32) Walter, M.; Kravchyk, K. V.; Bofer, C.; Widmer, R.; Kovalenko, M. V. Polypyrenes as high-performance cathode materials for aluminum batteries. *Adv. Mater.* **2018**, 30, 1705644–1705650.

(33) Xie, J.; Rui, X.; Gu, P.; Wu, J.; Xu, Z.; Yan, Q.; Zhang, Q. Novel conjugated ladder-structured oligomer anode with high lithium storage and long cycling capability. *ACS Appl. Mater. Inter.* **2016**, 8, 16932–16938.

(34) Zhao, Q.; Lu, Y.; Chen, J. Advanced organic electrode materials for rechargeable sodium-ion batteries. *Adv. Energy Mater.* **2017**, 7, 1601792–1601814.

(35) Sun, X.; Duffort, V.; Mehdi, B. L. Investigation of the mechanism of Mg insertion in birnessite in nonaqueous and aqueous rechargeable mg-ion batteries. *Chem. Mater.* **2016**, 28, 534–542.

(36) Mizuno, Y.; Okubo, M.; Hosono, E.; Kudo, T.; Ohishi, K.; Okazawa, A.; Kojima, N.; Kurono, R.; Nishimura, S.; Yamada, A. Electrochemical Mg^{2+} intercalation into a bimetallic CuFe prussian blue analog in aqueous electrolytes. *J. Mater. Chem. A* **2013**, 1, 13055–13059.

(37) Pan, B.; Huang, J.; Feng, Z.; Li, Z.; He, M.; Zhang, L.; Vaughey, J. T.; Bedzyk, M. J.; Fenter, P.; Zhang, Z.; Burrell, A. K.; Liao, C. Polyanthraquinone-based organic cathode for high-performance rechargeable magnesium-ion batteries. *Adv. Energy Mater.* **2016**, 6, 1600140–1600146.

(38) Liu, S.; Pan, G. L.; Yan, N. F.; Gao, X. P. Aqueous TiO_2/$Ni(OH)_2$ rechargeable battery with a high voltage based on proton and lithium insertion/extraction reactions. *Energy Environ. Sci*. **2010**, 3, 1732–1735.